The mesh-LBP: Computing Local Binary Patterns on Discrete Manifolds

Naoufel Werghi
Electrical & Computer Eng. Department
Khalifa University, UAE

Stefano Berretti, Alberto Del Bimbo, Pietro Pala
Department of Information Engineering
University of Firenze, Italy

Abstract

In this paper, we present a novel and original framework for computing Local Binary Pattern (LBP)-like patterns on a triangular mesh manifold. This framework, dubbed mesh-LBP can be adapted to all the LBP variants employed in 2D image analysis. As such, it allows extending the related techniques to mesh surfaces. First, we describe the foundations, the construction and the features of the mesh-LBP. In the experiments, we first show evidence of the presence of the "uniformity" aspect in the mesh-LBP patterns. Then, we show the mesh-LBP repeatability across different instances of same objects, reporting also the application of mesh-LBP to the problem of 3D texture-classification in comparison to standard 3D surface descriptors.

1. Introduction

Local Binary Pattern (LBP) is a local shape descriptor that has been introduced by Ojala et al. [16, 17] for the purpose of describing 2D textures. Its computational simplicity and discriminative power attracted the attention of the image processing community, and rapidly it found other applications in visual inspection, remote sensing, face recognition and motion analysis. However, all the LBP-based methods developed so far operate either on photometric information provided by 2D color images, or on geometric information in 2D depth images.

Triangular mesh manifold is a simple, compact and flexible format for encoding shape information widely used in many fields, such as animation, medical imaging, computer-aided design and many others. The recent advances in shape scanning and modeling also allowed the integration of both photometric and geometric information into a single support defined over a 2D mesh-manifold. Despite the abundance and the richness of mesh manifold modality, to the best of our knowledge, there is no a computational support that allows the computation of LBP on this format. Since LBP requires an ordered support for its computation, in our opinion the major factor that contributed in this deficiency is the lack of an intrinsic order in the triangular mesh manifold. On the contrary, computation of LBP on 2D images benefit of the implicit ordering of the 2D image array. In this paper, we address the challenge of computing LBP on a mesh manifold by proposing an original computational framework, which we dubbed mesh-LBP that allows the extraction of LBP-like patterns in a triangular mesh manifold. With this framework, we can therefore build on the current 2D LBP analysis methods, extending them to mesh manifolds as well as to the mesh modality that embeds both geometrical and photometric information.

The paper is organized as follows: In the remaining of this Section, first we provide an overview of the LPB literature, then the main features of our contribution are emphasized; In Sect. 2, we describe the technical foundation of the mesh-LBP, and extend it to a multi-resolution framework in Sect. 3; Then we present some experimental studies and we show different application scenarios of the mesh-LBP in Sect. 4. Finally, concluding remarks and future work are drawn in Sect. 5.

1.1. LBP: Overview

The original LBP operator [16] forms labels for the image pixels by thresholding a 3×3 neighborhood of each pixel with the center value, and considering the result as a binary number (Fig. 1). This number encodes the mutual relationship between the central pixel and its neighboring pixels. The histogram of the so obtained numbers can then be used as a texture descriptor. This operator is distinguished by its simplicity and its invariance to monotonic gray-level transformations. An extended version that can operate on different circular neighborhood sizes, also allowing sub-pixel alterations, was proposed in [17]. Other neighborhood variants appeared later, like the oriented elliptic neighborhood proposed by Liao et al. [13], which accounts for anisotropic information, and the multi-block LBP (MB-LBP) that compares averages of intensities of neighboring pixels rather than pixel values, in order to capture macrostructure features in the image [25]. Other versions have been proposed to improve the discriminative power, such as the ILBP [11] in which pixel values are compared with the neighborhood mean, and ELPB [9] which encodes,
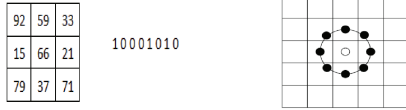
Figure 1. Left: computation of basic LBP code from a 3×3 neighborhood. Each pixel, starting from the upper left corner is compared with the central pixel to produce 1 if its value is greater and 0 otherwise. The result is an 8-bit binary code. Right: an example of circular neighborhood.

in addition to the binary comparison between pixels values, the amplitude of their difference using additive binary digits. To improve the robustness, Tan et al. [21] introduced the so-called local ternary pattern (LTP), which substitutes the original binary code by a 3-value code (1, 0 and -1) by means of a user-defined threshold. This new operator addressed the sensitivity to noise, though at the expense of the invariance to monotonic gray-level transformations. A fuzzy-logic version of the LTP was proposed later in [1], where a fuzzy membership function substituted the crisp three state association used in [21].

With regard to 3D shape analysis, most if not all the LBP-based approaches have been developed in the context of face recognition. All the techniques developed in this context operate on the standard depth images where the z coordinate is mapped to a gray-level value. This format allowed a straightforward employment of 2D LBP operators as it was demonstrated in the pioneering work of Li et al. [12]. Later, Huang et al. [8, 10] extended it to ELBP. Sandbach et al. [20] proposed local normal binary pattern (LBPN), which used the angle between normals at two points rather than the depth value. Fehr and Burkhardt [5] attempted an LBP tailored for volumetric data by sampling a sphere of a given radius around a central voxel. The approach is computationally expensive in that the rotation-invariance had to be addressed with complex techniques involving spherical correlation in the frequency domain.

1.2. Paper contribution

In this paper, we propose a framework, which we dubbed mesh-LBP for designing and extracting local binary patterns from a 2D mesh-manifold. In addition to its originality, this framework is characterized by the following features: 1) *Effectiveness*: This framework operates directly on 3D triangular mesh, thus avoiding expensive pre-processing, such as registration and normalization, required to obtain depth images; 2) *Generalization*: By its ability of handling mesh data, this framework can deal with a larger spectrum of surfaces (e.g., closed, open, self occluded) as compared to its counterpart in depth images; 3) *Adaptability*: This framework can be adapted to hold most if not all the LBP versions proposed for 2D and depth images; 4)

Simplicity: mesh-LBP preserves the simplicity of the original LBP, not requiring any surface parametrization, apart the standard mesh arrangement into facets and vertex arrays, while keeping linear computational complexity.

2. The mesh-LBP

The mesh-LBP is built upon the idea of establishing a local ordered arrangement in the mesh allowing to browse a ring of facets in a circular fashion.

Let $S(V, F)$ be the triangular mesh representation of an open or closed surface, where V and F are, respectively, the sets of vertices and facets in the mesh. Let consider a convex contour on a mesh, which we assume regular, i.e., each vertex has a valence of six. Consider the facets that have an edge on that contour (Fig. 2(a)). We dub these facets $Fout$ facets, as they seem pointing outside the contour. Let us consider also the set of facets that are one-to-one adjacent to the $Fout$ facets and which are located inside the convex contour. Each facet in this set, which we dub Fin, shares with its corresponding $Fout$ facet an edge located on the convex contour. Let assume that the $Fout$ facets are initially ordered in a circular fashion across the contour. Given that initial arrangement, we bridge the gap between each pair of consecutive $Fout$ facets, i.e., we extract the sequence of adjacent facets, located between the two consecutive $Fout$ facets and which share their common vertex (the vertex on the contour). We dub these facets $Fgap$ facets (Fig. 2(b)). In so doing, we obtain a ring of facets that are ordered in a circular fashion (Fig. 2(c)). The arrangement inherits the same direction (clock-wise or anti-clockwise) of the initial sequence of $Fout$ facets. The ring construction algorithm is described in the procedures "GetRing" (Algorithm 1) and "Bridge" (Algorithm 2).

Algorithm 1 – GetRing

Notation:

$Fout$: sequence of n facets, $fout_1, fout_2, \ldots, fout_n$, lying on a convex contour

Fin: sequence of n facets, $fin_1, fin_2, \ldots, fin_n$, one-to-one adjacent to $Fout$, and located inside the area delimited by the contour. Depending on the contour, the Fin might present duplication.

$Fgap_i$: sequence of adjacent facets located between a pair of consecutive $Fout$ facets $fout_i, fout_{i\%n+1}$, $i = 1, \ldots, n$, being % the modulo operator

Pseudocode:

   $Ring \leftarrow$ GetRing($Fout, Fin$)
   $Ring = [\ ]$
   for all pair $\langle fout_i, fout_{i\%n+1} \rangle$, $i = 1, \ldots, n$ **do**
     append $fout_i$ to $Ring$
     $Fgap_i \leftarrow$ Bridge($fout_i, fout_{i\%n+1}, fin_i$)
     append $Fgap_i$ to $Ring$
   end for

For the particular case of a contour formed by the three facet's edges, the $Fout$ facets represent the three facets adjacent to the central facet. In this case, the obtained
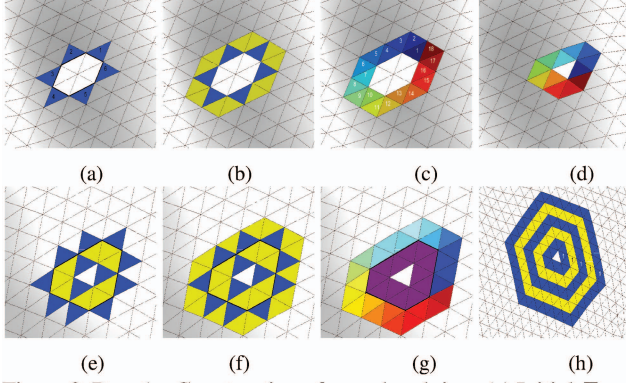
Figure 2. Row 1 – Construction of an ordered ring: (a) Initial $Fout$ facets; (b) Bridging the gap between the pairs of consecutive $Fout$ facets with the $Fgap$ facets; (c) The obtained ordered ring; (d) Ordered ring constructed around a central facet. Row 2 – Multi-resolution mesh-LBP construction: (e) Extraction of the next sequence of $Fout$ facets, as the facets adjacent to $Fgap$ and which are not part of the current ring; (f) Extracting the $Fgap$ facets; (g) The second ordered ring extracted; (h) Five concentric ordered rings. Notice that the first facet of each ring (marked by 1) is located at the same relative position. (Figure best seen on softcopy version.)

Algorithm 2 – Bridge

$Fgap_i \leftarrow$ Bridge($fout_i, fout_{i+1}, fin_i$)
$Fgap_i = [\,]$
$v \leftarrow$ vertex shared by $\langle fout_i, fout_{i+1} \rangle$
$gf \leftarrow$ facet adjacent to $fout_i$, different from fin_i, and containing v
$prev \leftarrow fout_i$
while $gf \neq fout_{i+1}$ **do**
    append gf to $Fgap_i$
    $new\_gf \leftarrow$ facet adjacent to gf, different from $prev$ and
                containing v
    $prev \leftarrow gf$
    $gf \leftarrow new\_gf$
end while

---

ring is composed of 12 ordered facets (Fig. 2(d)). Let $h(f) : S \rightarrow R$, be a scalar function defined on S, e.g., photometric data or curvature. The circular ordering of the facets allows us to derive a binary pattern (i.e., sequence of 0 and 1 digits) from it, and thus to compute a local binary operator in the same way as in the standard LBP. We define the basic mesh-LBP operator at a facet f_c by thresholding its ordered ring neighbourhood:

$$meshLBP(f_c) = \sum_{k=1}^{12} s(h(f_k) - h(f_c)) \cdot \alpha(k) \qquad (1)$$

$$s(x) = \begin{cases} 1 & x > 0 \\ 0 & x \leq 0 \, , \end{cases} \qquad (2)$$

where $\alpha(k)$ is a weighting function. For $\alpha(k) = 2^k$, we obtain the basic LBP operator firstly suggested by Ojala et al. [16]. Unless $\alpha(k)$ is a constant, different binary patterns and thus different mesh-LBP values can be derived from the central facet and its ring neighborhood.

In order to make the mesh-LBP invariant to the ordering of the facets in the ring and its traversal, two aspects should be addressed: The position of the first facet (i.e., the first $Fout$ facet) in the ring, that is which of the three facets adjacent to the central one the ring starts from; The direction of the ring traversal (clock-wise or anti-clockwise). The last aspect can be easily fixed by orienting the normals of the mesh-manifold. The first aspect can be addressed using three solutions: 1) Selecting the minimum binary pattern by performing a circular bit-wise shift as was suggested in the standard LBP [17]. However, this might affect the discriminative power of the operator. In addition, there is a strong hypothesis that the mesh-LBP patterns exhibit an "uniformity" aspect similar to the one observed by Ojala et al. [17] in their gray level images counterpart. This hypothesis is confirmed in the experiments reported in Sect. 4.1. Thus, we think that adopting the solution (1) might compromise the uniformity aspect; 2) Considering all binary pattern values, but this solution create redundancy and further burden the computation; 3) Selecting the first $Fout$ facet with respect to a local reference frame determined based on the local morphology of the ring neighborhood. For this purpose, the method proposed in [22] can be used. In the experiments, we adopted a solution close to this last one, where the nearest facet to the azimuth plane derived from the local reference frame of the ring is selected.

3. Multi-resolution mesh-LBP

The mesh-LBP is extended to a multi-resolution framework by deriving from the ordered ring a sequence of subsequent rings preserving the ordering property. From the first ring, the sequence of facets that are one-to-one adjacent to the $Fgap$ facets are extracted (Fig. 2(e)). This sequence, which inherits the order property of the $Fgap$ facets, will constitute the set of $Fout$ facets for the subsequent ring. So, by filling the gap between each two consecutive facets of this sequence (Fig. 2(f)), a new ring which exhibits the same ordered structure of its precedent is obtained (Fig. 2(g)). By iterating this procedure we build a sequence of concentric ordered rings which represent the primitive entity for computing multi-resolution mesh-LBP (Fig. 2(h)). Details of the corresponding algorithm ("Multi-Ring") are reported in Algorithm 3. In this case, the "GetRing" procedure is slightly modified, so that it produces the $Fgap$ facets of the current ring and the $Fout$ facets of the subsequent ring.

It is worth mentioning that in the case the regularity assumption for the mesh is satisfied, the number of facets ν across the rings evolves according to the following geometric progression from ring i to ring $i + 1$:

$$\nu_{i+1} = \nu_i + 12. \qquad (3)$$

Given a multi-ring constructed around a central facet f_c,

Algorithm 3 – Multi-Rings

Nr: Number of rings constructed around a central facet
$Rings \leftarrow [\ ]; Fin \leftarrow Fin\_root; Fout \leftarrow Fout\_root$
for $i = 1$ to Nr **do**
    $(Ring, NewFout, Fgap) \leftarrow \text{GetRing}(Fout, Fin)$
    Append $Ring$ to $Rings$
    $Fout \leftarrow NewFout$
    $Fin \leftarrow Fgap$
end for

a multi-resolution mesh-LBP operator is derived as follows:

$$meshLBP_p^r(f_c) = \sum_{k=1}^{p} s(h(f_k^r) - h(f_c)) \cdot \alpha(k), \quad (4)$$

where r is the ring number, and p is the number of facets equally spaced on the ring. The parameters r and p control, respectively, the radial resolution and the azimuthal quantization of the operator.

The repeatability of the mesh-LBP patterns can be hampered by the local mesh tessellation irregularity, for which the assumption of vertex valence of six does not hold, and consequently the regular progression of Eq. (3) is not satisfied. This issue can be addressed in different ways: 1) Adding a pre-processing stage that regularizes the density of the mesh triangulation; 2) Deriving iso-geodesic contours from the ordered rings that will act as a support region for computing mesh-LBP operators; 3) Applying the local density invariant smoothing, proposed by Darom and Keller [4] to the ring vertices around the central facet. In our experiments, we rather used a simple technique that interpolates the scalar function across each ring to obtain a sequence that matches the ideal progression.

Finally, we observe that the topology of the neighborhood from which the mesh-LBP features are computed can be changed to accommodate the specificities of a given shape analysis application. In fact, we can show that most, if not all, the different LBP neighborhood and operator variants proposed in the literature can be easily derived from the ordered rings structure of the mesh-LBP. Because of the limited space, we just mention the different LBP variants and illustrate the related mesh-LBP patterns in Tab. 1.

4. Experiments

In the experimentation, we examined three different aspects of the proposed framework: 1) Presence of mesh-LBP uniform patterns; 2) The repeatability of mesh-LBP patterns; 3) Discriminative capability of mesh-LBP for 3D texture patterns.

4.1. Uniform patterns

By studying the statistics of the number of bitwise 0-1 transitions in the binary patterns, Ojala et al. [17] no-

ticed that the majority of the patterns in textured 2D images have a number of transitions U equal at most to 2. These patterns are called "uniform". In our investigation, we considered a representative set of three surface mesh collected from different sources. The first surface is a portion of a pot object from the "MIT CSAIL textured 3D models database" [7]. This object exhibits textured shape patterns on the surface. The second surface represents a face scan from the "Binghamton University 3D facial expression database" (BU-3DFE) [24]. The third one is a closed surface of a cat model from the "TOSCA high-resolution database" [3]. These models are shown in Fig. 3(a)-(c), respectively.
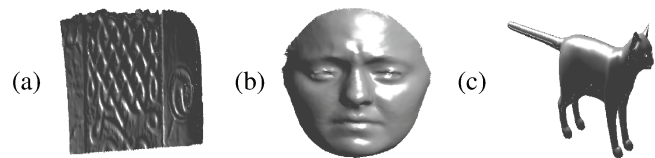

Figure 3. Mesh models used in the uniformity and surface description experiments: (a) Portion of a pot (MIT CSAIL textured 3D models); (b) Face surface (BU-3DFE); (c) Cat model (TOSCA high-resolution).

Four scalar functions on the mesh manifold have been studied, namely, the *mean* curvature (H), the *gaussian* curvature (K), the *curvedness* (C), and the *angle between facets normals* (D). For each of these functions, we computed the number of transitions U in the binary patterns computed by using the multi-resolution mesh-LBP operator of Eq. (4), across six levels of spatial resolution (from 1 to 6), and using 12 samples for the azimuthal quantization (in this case patterns are uniform for $U \leq 4$). The results are depicted in Fig. 4. We can observe that the number of uniform patterns exceeds 90% up to the third ring, across the four scalar functions, for all the three surfaces. The angle between normals is the function exhibiting the best uniformity with an overall percentage above 80%. The mean curvature and the curvedness show virtually the same rates. Overall, all the scalar functions show a percentage of uniform patterns above 70%. These observations suggest an evidence on the existence of a "uniformity" aspect in the triangular mesh manifold, and thus mesh-LBP has the potential of adapting the uniformity-driven description suggested by Ojala et al. [17].

4.2. Repeatability

Repeatability of mesh-LBP patterns measures the capability of the descriptor to assume comparable values when extracted from corresponding facets of different instances (i.e., scans) of a same 3D object. For this experiment, we acquired 32 facial scans of a same subject with neutral or moderate facial expressions. The four surface functions reported in Sect. 4.1, namely, *mean* curvature, *gaussian* cur-

LBP variant	Center-symmetric [6]	Local-line [19]	Archimedian Spiral [15]	Elongated [13]	Three-Patch [23]	Four-Patch [23]
mesh-LBP patterns						

Table 1. Different LBP variants and their corresponding patterns in the mesh-LBP.
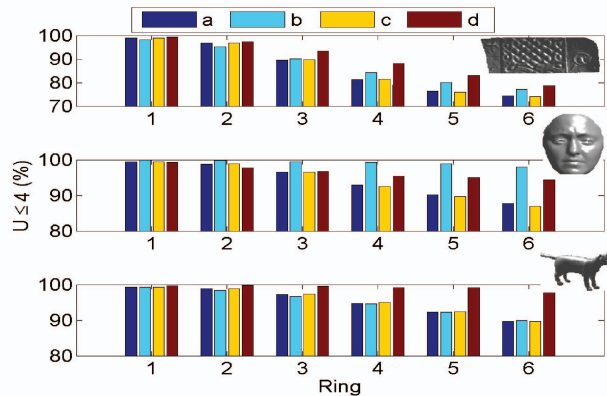

Figure 4. Percentage of facets having a number of transition U less than 3 in their mesh-LBP computed for the three mesh models of Fig. 3. Legend – a: Mean curvature; b: Gaussian curvature; c: Curvedness; d: Angle between facets normals.

vature, *curvedness* and *angle* between facets normals have been used for computing mesh-LBP. For each of these functions, we considered three different mesh-LBP operators, that is, $\alpha_1(k) = 1$, $\alpha_2(k) = 2^k$, and the *number of transitions*. Different spatial resolutions corresponding to eight rings $r = 1, \ldots, 8$ have been also accounted. To compute the repeatability of mesh-LBP patterns, we followed a similar approach to that proposed in [14] for 3D keypoints. With this solution, first fine alignment between each 3D probe scan and a reference gallery scan is performed using ICP registration. Then, for each facet in the probe, the nearest neighbor facet in the gallery is found whose mesh-LBP value is equal to the mesh-LBP value of the probe facet (the nearest neighbor distance between facets is computed using the 3D coordinates of their centroid). This operation is repeated for each facet in the probe and the distances computed as above are recorded. Varying a proximity radius around the facets it is possible to count the repeated mesh-LBP values between probe and gallery scans, which are away less than the radius. The overall repeatability is obtained by iteratively using one of the scan as gallery and all the remaining as probes. Figures 5(a)-(c) show the obtained average repeatability as a function of increasing values of the distance radius, respectively, for the three used mesh-LBP operators. Plots are reported for the 1st-ring, but a similar behaviour resulted for the other rings. In general,

we observe that the gaussian curvature and the angle between facets normals show a similar behaviour, obtaining the highest repeatability in all the cases. The mean curvature and curvedness, instead, score similar results each other, showing lower performance especially for the α_1 and α_2 weighting functions.

4.3. Discriminating 3D Texture Patterns

In this experiment, we investigated the potential of the mesh-LBP for discriminating 3D texture patterns on mesh-manifolds. We clarify that with "3D texture pattern" we do not mean texture-mapped mesh models, but 3D mesh surfaces exhibiting regular shape patterns. We also point out that our goal is not to elaborate a proper method for 3D shape texture classification, but rather probing the capability of the mesh-LBP as a framework for such task that, to the best of our knowledge, has not been addressed before.

We used surface samples exhibiting a variety of 3D shape patterns, collected from seven different object models of the "MIT CSAIL textured 3D models database" [7]. These objects are *bagel*, *bird*, *gargoyle*, *head*, *lion*, *plaque* and *pot*. These models have a reasonably uniform mesh, and the corresponding 3D textures are reported in Fig. 6 (1st row). For each sample, we computed a 1D-histogram of the mesh-LBP operator (Eq. (4)) for the weighting functions ($\alpha_1(k) = 1$) and ($\alpha_2(k) = 2^k$), for the spatial resolution $r = 1, \ldots, 7$, and azimuthal quantization $m = 12$. For the weighting function α_1, the resulting mesh-LBP patterns can take values in the interval [0,12], so these are accumulated in a 1-D histogram with 13 bins for each ring. For the α_2 function, for which the range of mesh-LBP patterns is [0,4096], we adopted a uniform/non-uniform mesh-LBP partition, that is 1123 bins corresponding to uniform patterns having number of transitions equal at most to four, and one bin for all the rest (the 2973 non-uniform ones). Based on this, two types of 2D histograms of size (7,13) and (7,1124), associated with α_1 and α_2, respectively, are computed for each texture model. The histograms are computed on an area of 19 rings, which is sufficient for covering the 3D texture variation in each texture sample.

To compute the distance between two histograms H_1 and H_2 the complement of the Bhattacharyya coefficient $B(.)$, i.e., $\sqrt{1 - B(H_1, H_2)}$ was used. We repeated the histogram computation for each model using four scalar func-
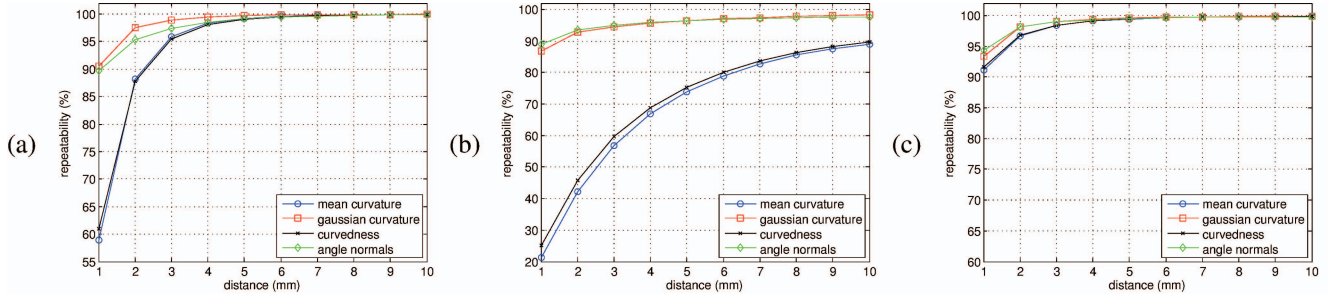
Figure 5. Repeatability of mesh-LBP: (a) $\alpha_1(k) = 1$; (b) $\alpha_2(k) = 2^k$; (c) number of transitions.

tions, namely, the *mean* curvature, the *gaussian* curvature, the *shape index* (instead of the *curvedness*) and the *angle* between facets normals. As an example, Fig. 6 (2nd row) depicts histogram instances, of the first type, obtained with the *angle* between facets normals.

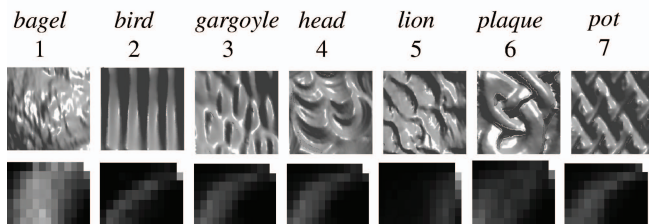| bagel	bird	gargoyle	head	lion	plaque	pot
1	2	3	4	5	6	7

Figure 6. Top: 3D texture samples from the seven classes. Bottom: The corresponding histograms obtained with the *angle* between facets normals using 7 rings and 12 samples per ring (histograms with 7 rows and 13 columns).

We compared the mesh-LBP descriptors with other standard descriptors, including the geometric histogram (GH) [2], and the shape distribution variants [18], that is the distance between a fixed point and one random point on the surface ($D1$), the distance between two random points on the surface ($D2$), the square root of the area of the triangle between three random points on the surface ($D3$), the cube root of the volume of the tetrahedron between four random points on the surface ($D4$), and the angle between three random points on the surface ($A3$).

The assessment of the discriminative power of the different descriptors is performed as follows. For each texture class, we have 30 instances and compute descriptors of each type. From the obtained set, we compute the mean and the variance. Since all the descriptors have a histogram structure, the variance we consider here is the variance of the Bhattacharyya distances between descriptor instances and their mean. For each descriptor we compute the distance matrix of the seven texture classes, where the diagonal term is the mean intra-class distance of the class i and the non-diagonal term is the distance between the two means of the the descriptors of the classes i and j.

Figure 7 and 8 depict, respectively, the distance matrices related to the mesh-LBP descriptors and the group of other standard descriptors. Due to space limit, we reported only the results for the Gaussian curvature (K) and the angle between facet normals (D). We notice that the intra-class distance is quite below the inter-class counterpart across all mesh-LBP descriptors. Whereas for the other standard descriptors we notice that the intra-class distance exceeds its inter-class counterpart at many instances (marked in bold). This is a clear indication of the potential and the appropriateness of the mesh-LBP descriptors for discriminating textured shapes as compared to other standard descriptors.

In Fig. 9 we also report the distance matrices between all the class instances (i.e., 30 instances for each of the 7 classes). In the top row, results for the mesh-LBP computed using K and D descriptors, and the weighting functions α_1 and α_2 are given in (a) and (b), respectively. In the bottom row, results for the standard descriptors are shown. In the mesh-LBP distance matrices, we can easily distinguish the 30×30 blocks related to the inter-class distances between class pairs. This is not straightforward for the other descriptors. This observation confirms the superior discriminant capability of the mesh-LBP descriptors. The classification accuracy, estimated as the percentage of occurrences where the inter-class distance is greater than the intra-class distance across all the classes is reported for each descriptor beneath the distance matrix in Fig. 9. The obtained results clearly evidence the performance improvement obtained using the mesh-LBP approach.

Finally, we compared the discriminative power of the mesh-LBP descriptors using the following criterion:

$$\mathcal{J} = \sum_{i=1}^{M} \sum_{j=i+1}^{M} \mathcal{D}_{ij}, \qquad (5)$$

where M is the number of texture classes (7 in our experiment). $\mathcal{D}_{ij}$ is the probabilistic-like inter-class separation between texture classes i and j defined as follows:

$$\mathcal{D}_{ij} = \frac{1}{2}dist(\bar{H}_i, \bar{H}_j)^2\left(\frac{1}{\sigma_{H_i}^2} + \frac{1}{\sigma_{H_j}^2}\right) + \frac{1}{2}\left(\frac{\sigma_{H_i}^2}{\sigma_{H_j}^2} + \frac{\sigma_{H_j}^2}{\sigma_{H_i}^2} - 2\right),$$

where $(\bar{H}_i, \bar{H}_j)$ and $(\sigma_{H_i}, \sigma_{H_j})$ are the mean histograms and the variances of the texture classes i and j, respectively.

(a) K

	1	2	3	4	5	6	7
1	0.01	0.16	0.17	0.08	0.31	0.07	0.16
2	0.00	0.02	0.12	0.18	0.36	0.16	0.15
3	0.00	0.00	0.01	0.19	0.38	0.15	0.06
4	0.00	0.00	0.00	0.01	0.26	0.09	0.18
5	0.00	0.00	0.00	0.00	0.03	0.32	0.39
6	0.00	0.00	0.00	0.00	0.00	0.02	0.14
7	0.00	0.00	0.00	0.00	0.00	0.00	0.05

	1	2	3	4	5	6	7
1	0.08	0.59	0.51	0.46	0.48	0.53	0.49
2	0.00	0.12	0.55	0.54	0.60	0.61	0.56
3	0.00	0.00	0.09	0.41	0.48	0.48	0.43
4	0.00	0.00	0.00	0.12	0.41	0.44	0.44
5	0.00	0.00	0.00	0.00	0.11	0.51	0.51
6	0.00	0.00	0.00	0.00	0.00	0.09	0.45
7	0.00	0.00	0.00	0.00	0.00	0.00	0.13

(b) D

	1	2	3	4	5	6	7
1	0.01	0.37	0.28	0.32	0.44	0.19	0.31
2	0.00	0.02	0.25	0.25	0.47	0.32	0.25
3	0.00	0.00	0.04	0.34	0.54	0.19	0.08
4	0.00	0.00	0.00	0.03	0.30	0.31	0.34
5	0.00	0.00	0.00	0.00	0.08	0.46	0.56
6	0.00	0.00	0.00	0.00	0.00	0.01	0.24
7	0.00	0.00	0.00	0.00	0.00	0.00	0.01

	1	2	3	4	5	6	7
1	0.08	0.57	0.49	0.55	0.58	0.58	0.54
2	0.00	0.13	0.54	0.51	0.60	0.62	0.53
3	0.00	0.00	0.12	0.48	0.61	0.46	0.36
4	0.00	0.00	0.00	0.12	0.43	0.52	0.47
5	0.00	0.00	0.00	0.00	0.17	0.61	0.61
6	0.00	0.00	0.00	0.00	0.00	0.08	0.42
7	0.00	0.00	0.00	0.00	0.00	0.00	0.15

Figure 7. Distance matrices between the 3D texture classes, related to α_1 (left) and α_2 (right), obtained using Gaussian curvature (K), and angle between facets normals (D).

The criterion $\mathcal{J}$ computed for the different mesh-LBP descriptors is reported in Tab. 2. We notice that for both the weighting functions, the descriptors keep the same performance ranking, with D descriptor coming at the top followed by the K, then come SI and H.

	H	K	SI	D
$\mathcal{J}(\alpha_1)$	9.84	49.73	10.22	93.02
$\mathcal{J}(\alpha_2)$	24.90	29.36	26.83	30.11

Table 2. Discriminative power $\mathcal{J}$ computed for the different mesh-LBP descriptors.

5. Conclusions

In this paper, we presented mesh-LBP as a novel framework for computing local binary patterns on triangular mesh manifold. This framework keeps the simplicity and the elegance characterizing the original LBP and allows the extension of all its variants, developed in 2D image analysis, to the mesh manifold. The mesh-LBP reliefs object surface data from normalization and registration procedure required when using depth images, while it extends the spectrum of LBP analysis to closed surfaces. The experimental tests revealed that mesh-LBP exhibit a kind of "uniformity" aspect for the different types of scalar functions, pretty similar to the one noticed in 2D LBP. Experiments on 3D texture classification showed clear evidence of the appropriateness of the mesh-LBP descriptors for such a task, and their superior discriminative power as compared to other popular descriptors. As future work, we plan extending the mesh-LBP to global analysis. One potential approach is extracting ordered blocks from the mesh surfaces and then construct from them, by concatenation, a global histogram. We believe that mesh-LBP will open new perspectives for mesh manifold analysis and will be an appropriate complement to other mesh manifold analysis techniques.

References

[1] T. Ahonen and M. Pietikäinen. Soft histograms for local binary patterns. In *Proc. Finnish Signal Processing Symp.*, pages 1–4, 2007. 2

[2] A. Ashbrook, R. Fisher, C. Robertson, and N. Werghi. Finding surface correspondance for object recognition and registration using pairwise geometric histograms. In *Proc. European Conf. on Computer Vision*, pages 674–686, Friburg, Germany, June 1998. 6

[3] A. Bronstein, M. Bronstein, and R. Kimmel. Numerical geometry of non-rigid shapes. *Springer-Verlag, New-York*, 2008. 4

[4] T. Darom and Y. Keller. Scale-invariant features for 3-D mesh models. *IEEE Trans. on Image Processing*, 21(5):2758–2769, 2012. 4

[5] J. Fehr and H. Burkhardt. 3D rotation invariant local binary patterns. In *Proc. Int. Conf. on Pattern Recognition*, pages 1–4, 2008. 2

[6] M. Heikkilä, M. Pietikäinen, and C. Schmid. Description of interest regions with local binary patterns. *Pattern Recognition*, 42(3):425–436, 2009. 5

[7] http://people.csail.mit.edu/tmertens/textransfer/data/. 4, 5

[8] D. Huang, M. Ardabilian, Y. Wang, and L. Chen. 3-D face recognition using eLBP-based facial description and local feature hybrid matching. *IEEE Trans. on Information Forensics and Security*, 7(5):1551–1565, 2012. 2

[9] D. Huang, Y. Wang, and Y. Wang. A robust method for near infrared face recognition based on extended local binary pattern. In *Proc. Int. Symp. on Visual Computing*, pages 437–446, 2007. 1

[10] Y. Huang, Y. Wang, and T. Tan. Combining statistics of geometrical and correlative features for 3D face recognition. In *Proc. British Machine Vision Conf.*, pages 879–888, 2007. 2

[11] H. Jin, Q. Liu, H. Lu, and X. Tong. Face detection using improved LBP under bayesian framework. In *Proc. Int. Conf. on Image Graphics*, pages 306–309, 2004. 1

[12] S. Li, C. Zhao, M. Ao, and Z. Lei. Learning to fuse 3D+2D based face recognition at both feature and decision levels.

(a) GH	1	2	3	4	5	6	7
1	0.68	**0.65**	**0.58**	**0.52**	0.77	**0.61**	**0.50**
2	0.00	0.47	0.49	0.51	0.68	0.63	0.82
3	0.00	0.00	0.49	**0.39**	0.66	0.59	0.73
4	0.00	0.00	0.00	0.37	0.66	0.61	0.65
5	0.00	0.00	0.00	0.00	0.26	0.70	0.77
6	0.00	0.00	0.00	0.00	0.00	0.68	0.73
7	0.00	0.00	0.00	0.00	0.00	0.00	0.46

(b) $D1$	1	2	3	4	5	6	7
1	0.11	0.15	0.13	0.21	0.37	0.27	**0.06**
2	0.00	0.16	0.22	0.28	0.50	0.41	**0.13**
3	0.00	0.00	0.11	0.14	0.33	0.24	0.17
4	0.00	0.00	0.00	0.11	0.37	0.28	0.25
5	0.00	0.00	0.00	0.00	0.13	0.15	0.41
6	0.00	0.00	0.00	0.00	0.00	0.11	0.32
7	0.00	0.00	0.00	0.00	0.00	0.00	0.10

(c) $D2$	1	2	3	4	5	6	7
1	0.12	0.29	0.13	0.16	0.15	**0.10**	**0.04**
2	0.00	0.12	0.40	0.42	0.39	0.37	0.28
3	0.00	0.00	0.14	0.14	0.16	**0.12**	0.14
4	0.00	0.00	0.00	0.11	0.18	0.11	0.18
5	0.00	0.00	0.00	0.00	0.10	0.12	0.15
6	0.00	0.00	0.00	0.00	0.00	0.11	0.11
7	0.00	0.00	0.00	0.00	0.00	0.00	0.14

(d) $D3$	1	2	3	4	5	6	7
1	0.17	**0.10**	0.49	0.75	0.61	0.59	**0.12**
2	0.00	0.20	0.45	0.71	0.56	0.55	**0.16**
3	0.00	0.00	0.18	0.32	0.18	**0.14**	0.56
4	0.00	0.00	0.00	0.19	**0.18**	0.20	0.80
5	0.00	0.00	0.00	0.00	0.19	**0.08**	0.66
6	0.00	0.00	0.00	0.00	0.00	0.18	0.65
7	0.00	0.00	0.00	0.00	0.00	0.00	0.17

(e) $D4$	1	2	3	4	5	6	7
1	0.06	**0.04**	0.47	0.74	0.52	0.56	0.12
2	0.00	0.05	0.47	0.74	0.52	0.55	0.10
3	0.00	0.00	0.19	0.40	**0.11**	**0.12**	0.54
4	0.00	0.00	0.00	0.29	0.32	0.38	0.78
5	0.00	0.00	0.00	0.00	0.24	**0.14**	0.58
6	0.00	0.00	0.00	0.00	0.00	0.17	0.61
7	0.00	0.00	0.00	0.00	0.00	0.00	0.03

(f) $A3$	1	2	3	4	5	6	7
1	0.27	**0.22**	**0.21**	**0.23**	**0.19**	**0.22**	**0.13**
2	0.00	0.23	**0.08**	**0.07**	**0.12**	**0.09**	0.31
3	0.00	0.00	0.23	**0.07**	**0.09**	**0.06**	0.29
4	0.00	0.00	0.00	0.21	**0.11**	**0.07**	0.31
5	0.00	0.00	0.00	0.00	0.21	**0.08**	0.26
6	0.00	0.00	0.00	0.00	0.00	0.23	0.30
7	0.00	0.00	0.00	0.00	0.00	0.00	0.28

Figure 8. Distance matrices related to the Geometric Histogram, and the five shape distribution descriptors, $D1$, $D2$, $D3$, $D4$, $A3$.

(a) α_1 K: 100%   D: 100%   (b) α_2 K: 100%   D: 100%

GH: 90.3% D1: 95.9% D2: 93.6% D3: 91.6% D4: 93.9% A3: 77.0%

Figure 9. Distance matrices for class instances. Top row: mesh-LBP computed using K and D descriptors and the functions (a) α_1, and (b) α_2. Bottom row: standard descriptors. For each case, the average classification accuracy is also reported in percentage.

In *Proc. Int. Work. on Analysis and Modeling of Faces and Gestures*, pages 44–54, 2005. 2

[13] S. Liao and A. Chung. Face recognition by using elongated local binary patterns with average maximum distance gradient magnitude. In *Proc. Asian Conf. on Computer Vision*, pages 672–679, 2007. 1, 5

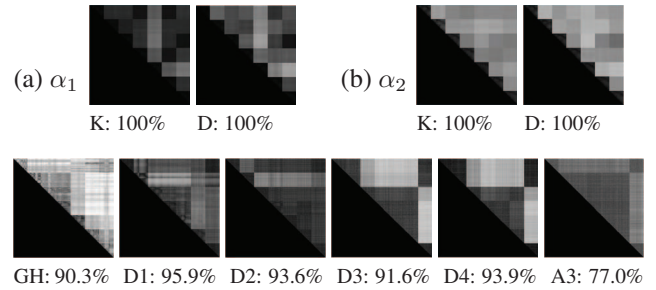[14] A. S. Mian, M. Bennamoun, and R. Owens. Keypoint detection and local feature matching for textured 3D face recognition. *Int. Journal of Computer Vision*, 79(1):1–12, Aug. 2008. 5

[15] L. Nanni, A. Lumini, and A. Brahnam. Local binary patterns variants as texture descriptors for medical image analysis. *Artificial Intelligence in Medecine*, 49:117–125, 2010. 5

[16] T. Ojala, M. Pietikäinen, and D. Harwood. A comparative study of texture measures with classification based on featured distribution. *Pattern Recognition*, 29(1):51–59, 1996. 1, 3

[17] T. Ojala, M. Pietikäinen, and T. Mäenpää. Multiresolution gray-scale and rotation invariant texture classification with local binary patterns. *IEEE Trans. on Pattern Analysis and Machine Intelligence*, 24(7):971–987, July 2002. 1, 3, 4

[18] R. Osada, T. Funkhouser, B. Chazelle, and D. Dobkin. Shape distributions. *ACM Trans. on Graphics*, 21(4):807–832, October 2002. 6

[19] A. Petpon and S. Srisuk. Face recognition with local line binary pattern. In *Proc. Int. Conf. on Image and Graphics*, pages 533–539, 2009. 5

[20] G. Sandbach, S. Zafeiriou, and M. Pantic. Local normal binary patterns for 3D facial action unit detection. In *Proc. IEEE Int. Conf. on Image Processing*, pages 1813–816, 2012. 2

[21] X. Tan and B. Triggs. Enhanced local texture feature sets for face recognition under difficult lighting conditions. In *Proc. Int. Work. on Analysis and Modelling of Faces and Gestures*, pages 168–182, 2007. 2

[22] F. Tombari, S. Salti, and L. Di Stefano. Unique signature of histograms for local surface description. In *Proc. European Conf. on Computer Vision*, volume 3, pages 347–360, Crete, Greece, 2010. 3

[23] L. Wolf, T. Hassner, and Y. Taigman. Descriptor based methods in the wild. In *Proc. ECCV Work. on Faces in Real-Life Images*, pages 1–14, 2008. 5

[24] L. Yin, X. Wei, Y. Sun, J. Wang, and M. Rosato. A 3D facial expression database for facial behavior research. In *Proc. IEEE Int. Conf. on Automatic Face and Gesture Recognition*, pages 211–216, Southampton, UK, 2006. 4

[25] L. Zhang, R. Chu, S. Xiang, and S. Li. Face detection based on multi-block LBP representation. In *Proc. Int. Conf. on Biometrics*, pages 11–18, 2007. 1